stellarator news

Published by Fusion Energy Division, Oak Ridge National Laboratory
Building 9201-2 P.O. Box 2009 Oak Ridge, TN 37831-8071, USA

Editor: James A. Rome Issue 79 January 2002
E-Mail: jar@ornl.gov Phone (865) 574-1306
On the Web at *http://www.ornl.gov/fed/stelnews*

Determination of line emission locations using the Zeeman effect in LHD

For the measurement of neutral atom density in the plasma edge region, the emission line intensity is a useful source of information. In conventional spectroscopy, we measure the intensity of an emission line integrated over the line of sight. When we can assume, say, cylindrical symmetry, we can convert the measured chord dependence of the emission line intensities to the radial distribution of the intensity. Even in a cylindrically symmetric plasma, this conversion may not be valid for the neutral atom influx, because the distribution of the neutral atoms depends on the structure of the plasma vessel and on the mode of operation of the plasma. For plasmas in divertor-configuration tokamaks and helical devices, the cylindrical symmetry assumption is not valid even for the plasma. We thus seek to develop a method to determine local intensities from the line-integrated emission intensity. One candidate for such a method is the Zeeman splitting of spectral lines. Work in this direction on the Alcator C-Mod tokamak has been recently reported [1]. Here we report our attempt to apply the method to the Large Helical Device (LHD).

Emission from the LHD plasma was observed with a set of parallel optical fibers, the lines of sight of which cover the entire cross section of the plasma elongated in the major radial direction, as shown in Fig. 1. Each line of sight is collimated by a lens to have a cylindrical shape about 30 mm in diameter. Optical fibers 5 m in length guide the collected UV and visible light to a spectrometer. The end surfaces of the fibers are aligned along the entrance slit of the spectrometer such that chord-resolved spectra are recorded on a CCD detector.

We first attempted to measure the Balmer-α line of neutral hydrogen but instantly encountered difficulties. The Zeeman splitting of the line profile is unclear because of the Doppler broadening and the rather complicated Zeeman effect that results from the intermediate strength of the magnetic field. We have thus chosen the HeI λ = 728.1-nm $2\,^1P - 3\,^1S$ line. The main reasons are that the transition is between singlet levels, so the line splitting is simply expressed by the normal Zeeman effect, and that the apparent line splitting is larger for the longer wavelength lines (the shifts of the σ components are proportional to the square of the wavelength of the line). Furthermore, Doppler broadening has been found to be smaller for helium than for hydrogen. The higher temperature of hydrogen atoms may be due to the existence of atoms produced from the dissociation of molecules.

The measurement was carried out for a 20-s stationary phase of a helium discharge heated by 25-s neutral beam injection (NBI). The nominal field strength B_{ax} was 2.75 T and the radius of the magnetic axis R_{ax} of the discharge was 3.6 m. The actual field strength at the plasma center in this cross section was 2.67 T. The NBI power was 1.2 MW. The gas fueling rate was controlled so as to keep the line-averaged electron density $\overline{n}_e$ constant. In the stationary phase, $\overline{n}_e$ was 3×10^{19} m^{-3}, and the electron temperature was 2 keV at the plasma center.

In this issue . . .

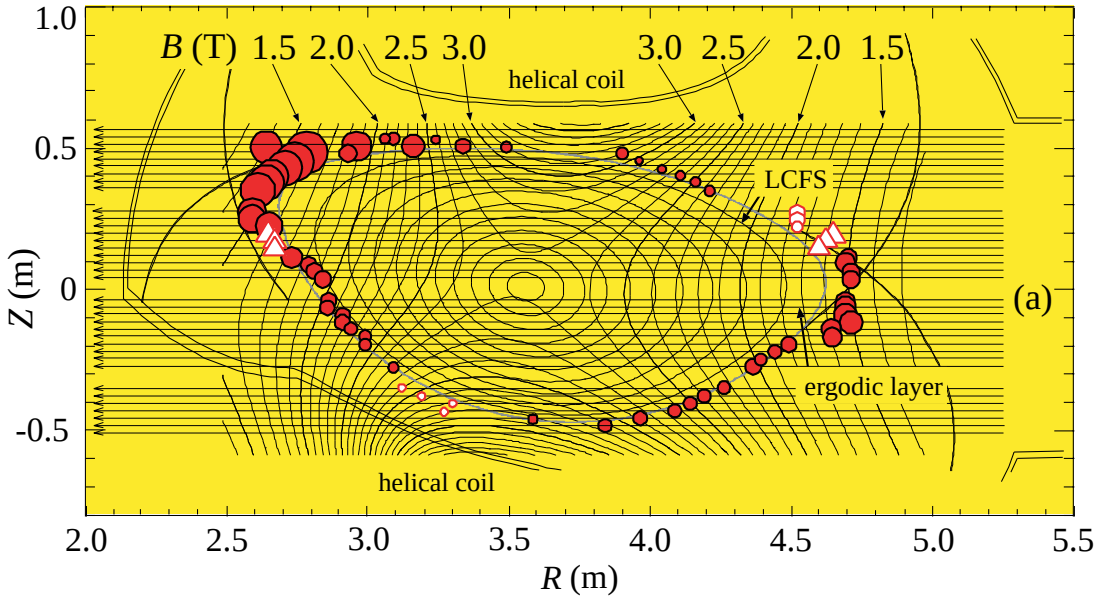

Fig. 1. Map of the magnetic surfaces and field strength for a configuration with R_{ax} = 3.6 m and B_{ax} = 2.75 T. The *R*- and *Z*-axes indicate the major radial direction and the direction perpendicular to the equatorial plane, respectively. Viewing chords are shown by the arrows. The circles and the triangles indicate the location of λ = 728.1 nm line emission and their size indicates the intensity of the emission. The symbols are explained in the text.

Figure 2 shows an example of the observed line profiles on the viewing chord (a) in Fig. 1. Although this line is subjected to the normal Zeeman effect, since the transition is between the singlet terms, the observed profile shows a rather complicated structure. This profile can be understood as the superposition of two Zeeman profiles that originate from different locations on the same viewing chord and are relatively shifted.

Since the viewing chord is almost perpendicular to the direction of the magnetic field, each Zeeman profile

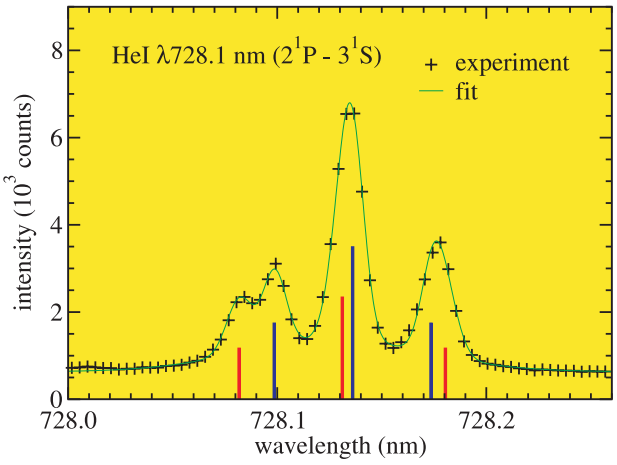

Fig. 2. Emission line profile of HeI, λ = 728.1 nm (2^1P – 3^1S), observed with viewing chord (a) in Fig. 1. The solid line is the result of a least-squares fit with two sets of Zeeman profiles plus a broad Gaussian profile.

should consist of one π component and two half-amplitude σ components that are symmetrically shifted from the π component. Under these constraints we perform a least-squares fitting for the profile with two sets of Zeeman profiles (six Gaussian profiles) plus a broad Gaussian profile. Each profile has an independent amplitude, width, and center wavelength. The result is shown in Fig. 2 as a dashed green line. The position and the height of the vertical bars respectively show the wavelength and the relative intensity of each of the Zeeman components. In this case, the broad Gaussian component has a FWHM (Doppler temperature) of 0.12 nm (19 eV) and is about 24% of the total intensity. The source of this component is not positively identified but is probably due to charge-exchange collisions or the recombining plasma component.

The derived field strength values from the sharp Zeeman profiles are *B* = 1.9 T and 1.51 T. The relative shift is 5.0×10^{-3} nm. The variation of the field strength along the viewing chord is shown in Fig. 3. Here, the derived field strength values are indicated by horizontal dashed lines. Each value has two candidates for spatial location. Candidates *R* = 2.46 m for *B* = 1.51 T and *R* = 4.33 m for *B* = 1.99 T are discarded because the former position is too far from the plasma boundary and the latter is deep inside the main plasma (see Fig. 1). We thus conclude that the spatial locations are *R* = 4.70 m for the former and *R* = 2.85 m for the latter. The result of this identification is shown in Fig. 1 with filled circles. Through similar analysis for all of the viewing chords, we reach a unique identification of the positions in most cases, as given in Fig. 1. However,

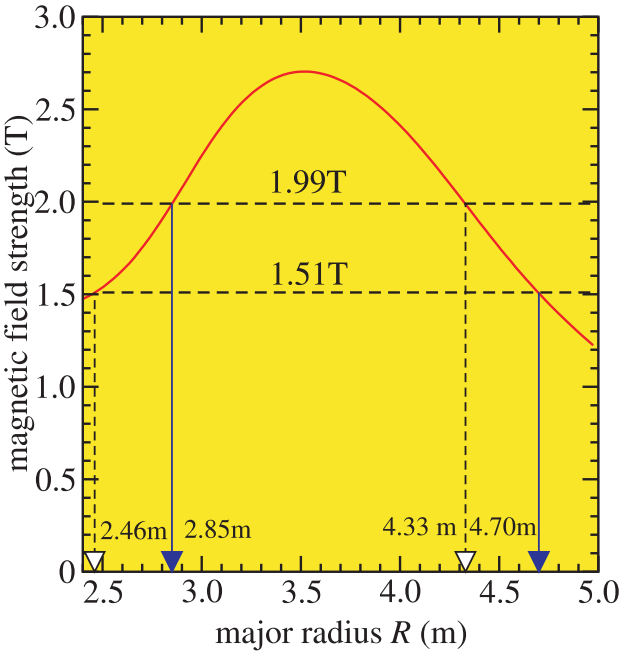

Fig. 3. Variation of magnetic field strength along viewing chord (a) in Fig. 1. The field strengths derived from the line profile for this viewing chord are shown by the horizontal dashed lines. The identified radial positions are shown by the vertical solid lines with arrows.

ambiguity remains for several viewing chords, which are indicated in Fig. 1 with the open triangles; the two magnetic field values are too close. The open circles indicate the derived field strength values with an uncertainty of about 0.05 T, which is due to the weak signals or the blending of impurity lines. The size of the symbol is proportional to the signal intensity; it is seen that very intense emissions are observed near the inner X point.

Figure 4 shows the relative speed of the atoms, which is obtained from the relative shift of two Zeeman profiles. The emission at the smaller major radius always shifts to the shorter wavelength with respect to that at the larger major radius. Unfortunately, we could not determine the absolute shift. This figure, especially the points for $Z \le 0$, suggests that the atoms have an inward motion with speeds of (1–2) $\times 10^3$ m/s. The dotted lines show the expected values of the apparent relative velocities under the assumption that the atoms have a monoenergetic velocity of 1.4×10^3 m/s, which corresponds to a thermal velocity of 300 K in the direction normal to the plasma boundary surface.

Figure 1 indicates that the regions of intense line emission form a closed zone, which almost coincides with the outer boundary of the ergodic layer, except for the "dent" near $Z = 0.05$ m, $R = 2.8$ m. We do not have any explanation for this at present. We consider the emission intensity and the decay of the atom density in the inward atom flux by a

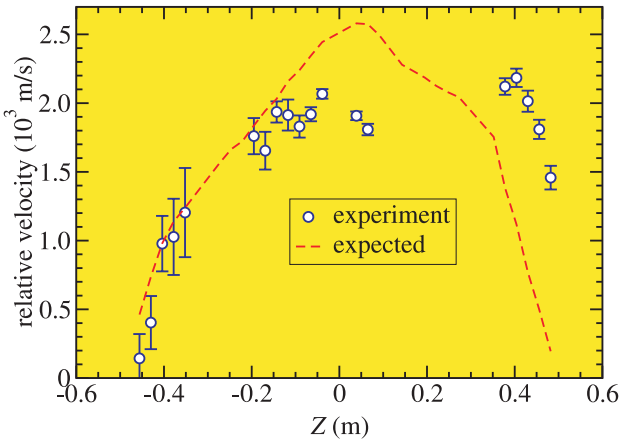

Fig. 4. The chord dependence of the apparent relative speed of the two components of atoms, which is derived from the Doppler shift of the observed emission line.

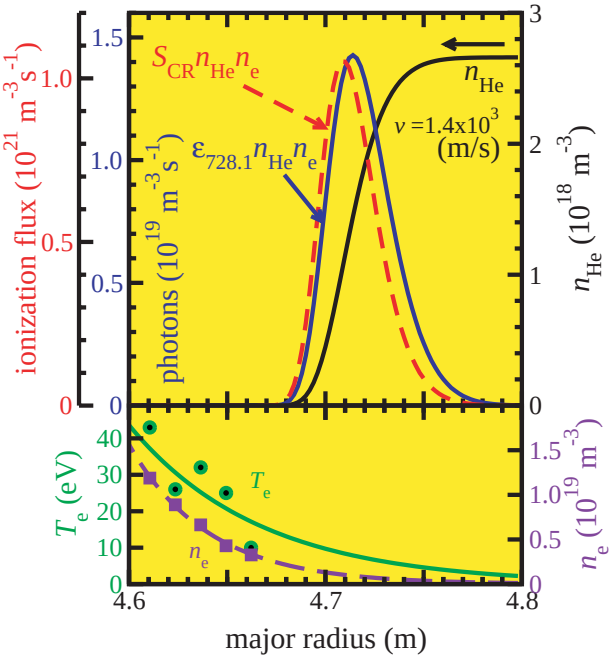

Fig. 5. Profiles of helium atom density n_{He}, the emission intensity of the 728.1 nm line $\varepsilon_{728.1} n_e n_{He}$, and the ionization flux $S_{CR} n_e n_{He}$ in a one dimensional penetration model with the mono-energetic penetration velocity of 1.4×10^3 m/s. The n_e and T_e profiles are extrapolated exponentially from values measured with Thomson scattering for a similar discharge.

one-dimensional model. The atom density n_{He} at the penetration depth ℓ in the x-direction is expressed as

$$n_{HE} = n_0 \exp\left[-\int_0^{\ell} \frac{n_e S_{CR}}{v} dx\right], \quad (1)$$

where S_{CR} and v are the effective ionization rate coefficient and the penetration velocity of the atoms, respectively, and n_0 is the atom density at the edge.

By using S_{CR} values obtained from the collisional-radiative (CR) model calculations [2], we evaluate Eq. (1) numerically for positions near the outer X-point on viewing chord (a) in Fig. 1. For n_e and T_e profiles the Thomson scattering data for a similar discharge of the same configuration are extrapolated with an exponential decay, as shown in Fig. 5. The penetration velocity v is assumed to be 1.4×10^3 m/s. At the same time we calculate the emission rate coefficient for the λ = 728.1-nm $\varepsilon_{728.1}$ with the CR model and integrate the emission intensity over the penetration path. From the observed value of $I_{728.1}$ (Fig. 1) we determine n_0 to be 2.7×10^{18} m^{-3}. The result is shown in Fig. 5. The spatial dependences of $\varepsilon_{728.1} n_e n_{He}$ and $S_{CR} n_e n_{He}$ are also shown. Both profiles have similar peaked shapes of about 3.5 cm in FWHM. This width of the emission intensity profile is consistent with the experimental result, which suggests that the extent of the emission region is about 5 cm or a little less. The radial location of the emission is also in good agreement with the experiment. The atom density is found to decay in the region of strong emission intensity before reaching the last closed flux surface (LCFS), which is located at R = 4.5 m.

M. Goto
National Institute for Fusion Science
Toki 509-5292, Japan
E-mail: goto@nifs.ac.jp

References

[1] J. L. Weaver et al., Rev. Sci. Instrum. **71**, 1664 (2000).

[2] B. L. Welch et al., Phys.\ Plasmas **8**, 1253 (2001).

[3] T. Fujimoto, J. Quant. Spectrosc. Radiat. Transfer **21**, 439 (1979).

[4] M. Goto and T. Fujimoto, Collisional-Radiative Model for Neutral Helium in Plasma Excitation Cross Section and Singlet-Triplet Wavefunction Mixing, NIFS-DATA-43, National Institute for Fusion Science, Toki, Japan (1997).

Quasi-Poloidal Stellarator development

The Quasi-Poloidal Stellarator (QPS) is being developed to study compact stellarators with very low aspect ratio ($\langle R \rangle / \langle a \rangle \sim 2.7$) in which the dominant components in the magnetic field spectrum are poloidally symmetric in field-line ("Boozer") coordinates. This leads to small $\boldsymbol{B} \times \nabla B$ drifts out of a flux surface and reduced neoclassical transport at low collisionality. The magnetic configuration may also have reduced poloidal viscosity, allowing larger poloidal flows, and relative insensitivity of the magnetic configuration to increasing beta. The device specifications for the proposed QPS are $\langle R \rangle$ = 0.9 m, $\langle a \rangle$ = 0.33 m, and $\langle B_{axis} \rangle$ = 1 T for a 1-s pulse, with 1-MW electron cyclotron heating (ECH) and 3-MW ion cyclotron resonant frequency (ICRF) for plasma heating.

The experiment is designed to study key issues for very low R/a, quasi-poloidal stellarators:

- anomalous transport, internal transport barriers, and flow shear in low-R/a configurations with quasi-poloidal symmetry;
- reduction of neoclassical transport resulting from near alignment of $\boldsymbol{B}$ and ∇B;
- impact of poloidal flows on enhanced confinement;
- equilibrium quality (islands, ergodic regions) and its repair at $R/a \sim 2.7$;
- robustness with plasma pressure, β, and dependence of bootstrap current on configuration properties; and
- ballooning stability limits and limiting mechanisms for quasi-poloidally symmetric configurations at very low R/a for $\langle \beta \rangle$ up to ~ 2.5%.

An earlier version of the QPS design was described in the November 2000 issue (No. 72) of *Stellarator News* (Physics Issues for Compact Drift-Optimized Stellarators), and the successful April 2001 Physics Validation Review (PVR) of the QPS proposal was described in the July 2001 issue (No. 76) of *Stellarator News* (Status of the QPS Project). While the basic QPS concept has not changed much this year, there has been substantial progress in improving the QPS plasma and coil configuration. The effort in 2001 focused on both improving the neoclassical confinement and increasing the space in the open central bore for a more feasible modular coil configuration.

The QPS plasma and coil configuration

The two-field-period QPS plasma configuration and the filamentary modular coils that create it are shown in Fig. 1. QPS has a racetrack configuration with 16 modular coils, 4 of each type. The four filamentary "coils" in the middle of the long sides are really two coils that are split, with each "coil" having half the current of the other modu-

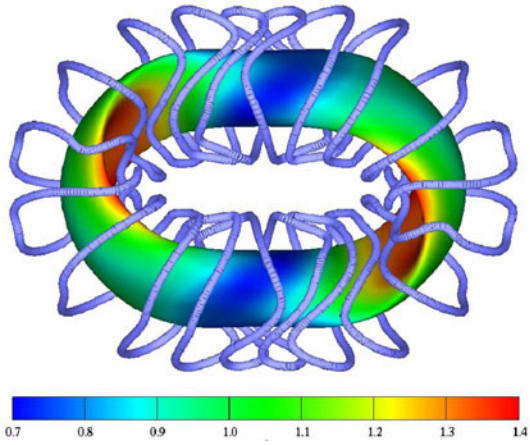

Fig. 1. Top view of the QPS plasma and coil configuration.

lar coils. The colors indicate the strength of $B \equiv |\boldsymbol{B}|$ in tesla on the last closed flux surface (LCFS); the value of B varies by a factor of 2 over the LCFS in Fig. 1. Side views from the middle of the long side and the end are shown in Fig. 2.

Figure 3 shows cross sections of the flux surfaces for a number of toroidal angles in half a field period. The colors indicate the same values of B as in Figs. 1 and 2, and the curves shows contours of B. The B contours are parallel (tokamak-like) for about half of each field period and become closed (more like the flux surfaces) near the D-shaped cross section in the middle of the long side. The LCFS for the QPS configuration is more rounded and does not exhibit the sharp edge of the PVR QPS configuration.

The pattern of the B contours on the LCFS is approximately poloidally banded in Figs. 1 and 2. The extent of the poloidal symmetry can be better seen by displaying B in field-line coordinates in which the magnetic field lines are straight lines. In this coordinate system, the magnitude of the magnetic field can be expressed in a Fourier series as

$$B = \Sigma\, B_{mn}(\psi) \cos(m\theta - n\phi),$$

where θ and ϕ are poloidal and toroidal angle variables and ψ is the toroidal flux. The dominant B_{mn} coefficients are shown in Fig. 4 vs the normalized plasma radius $\rho \equiv \psi^{1/2}$. For interior magnetic surfaces away from the plasma boundary ($\rho = 1$), the spectrum is dominated by the $m = 0$, $n = 1$ (in field period units) "linked-mirror" component; that is, B exhibits approximate poloidal symmetry, $\partial B/\partial\theta \approx 0$. Near the edge, there is a $1/R$ component ($m = 1$, $n = 0$), of comparable magnitude to the $m = 0$, $n = 1$ component, which violates the quasi-poloidal symmetry. In addition, there is a smaller helical component near the edge which decays away inside the plasma. This structure is similar to that in the large-A_p Wendelstein 7-X associated with omnigeneity-optimized transport. (Here, A_p is the geometric aspect ratio R/a.) However, the cancellation of the bootstrap current in W 7-X that occurs over the entire plasma cross section is not present in the QPS design. The effective magnetic aspect ratio based on the $m = 1$, $n = 0$ component of B (the $1/R$ field) is $A_{p,magnetic} \sim 5$, which is $2A_p$. This indicates a reduction in the grad B drift associated with this component of B. A substantial magnetic field ripple is associated with the mirror field component, corresponding to a mirror ratio (B_{max}/B_{min}) ~ 2 for the QPS configuration.

In the limit of *exact* poloidal symmetry, the canonical angular momentum $p_\theta = mv_\theta + eA_\theta$ is conserved. Particle orbit excursions would be limited to the gyroradius in the *toroidal* field, which is usually much smaller than the *poloidal* gyroradius (banana width) characteristic of orbit widths in axisymmetric devices. This reduction in orbit size implies a concomitant reduction in the bootstrap current compared to that in tokamaks. Thus QPS tends to operate either with a bootstrap current significantly lower than that in axisymmetric devices (for the same ι, or $1/q$, the potential reduction is ~ι/N) and/or at lower ι (higher q). Note that the implied smaller poloidal flux in QPS does not necessarily lead to increased neoclassical losses because the limiting orbit size is the toroidal gyroradius, which remains quite small.

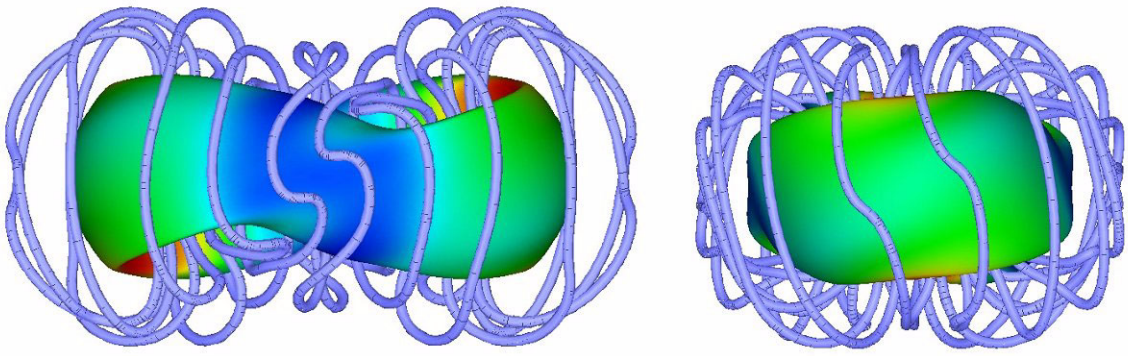

Fig. 2. Side views of the QPS plasma and coil configuration.

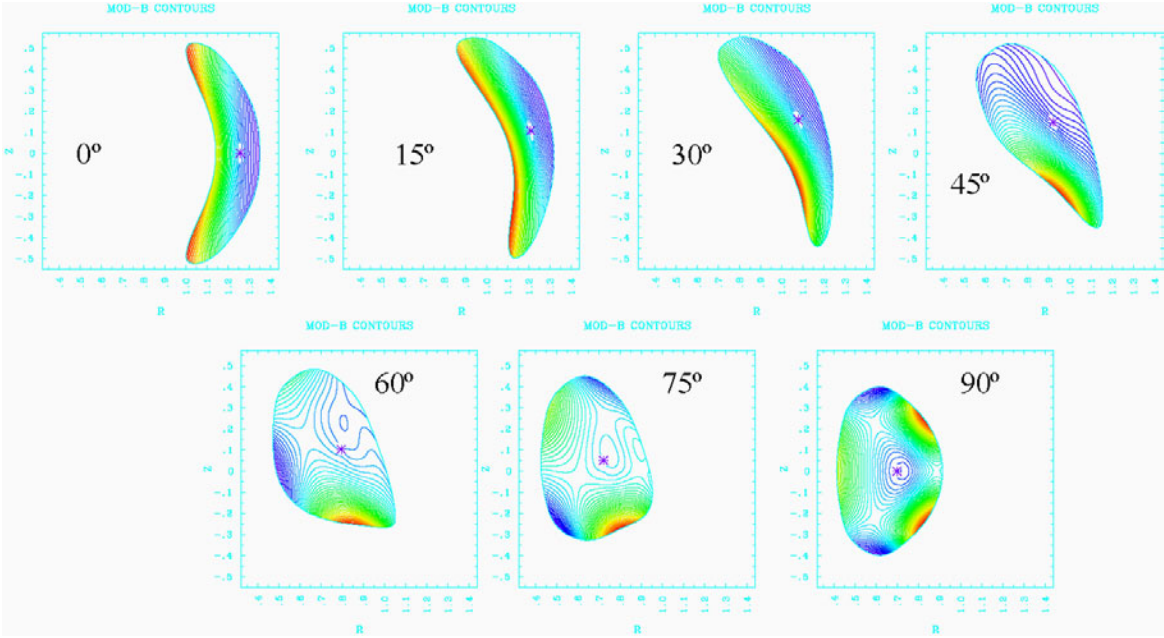

Fig. 3. Cross sections through the QPS flux surfaces at different toroidal angles showing contours of constant $|\boldsymbol{B}|$. Red is the highest field strength, and blue is the lowest.

Poloidally symmetric plasmas are, in field-line coordinates at least, similar to "linked mirrors" without end losses (which are eliminated by the toroidal geometry). However, because of the finite rotational transform in QPS, the magnetic field lines are generally ergodically distributed over the magnetic surface (except at rational surfaces), making the transport and stability properties of QPS plasmas more closely related to those of other quasi-symmetric stellarators than to those of mirror-like devices such as the Elmo Bumpy Torus.

The degree of quasi-poloidal symmetry can be better understood from Fig. 5, which shows the B contours (blue and purple curves) and magnetic field lines (red straight lines) for QPS on the magnetic flux surfaces $\rho = r/a = 0.1$ and 0.5, where r is the average radius of a flux surface. Since the radial motion of particles is given by the $\boldsymbol{B} \times$ grad B drift, the approximate alignment of $\boldsymbol{B}$ and grad B directions implies a suppression of these drift effects *away* from the magnetic surfaces. This has the potential to significantly reduce both the neoclassical energy and the particle losses as well as the self-consistent bootstrap current.

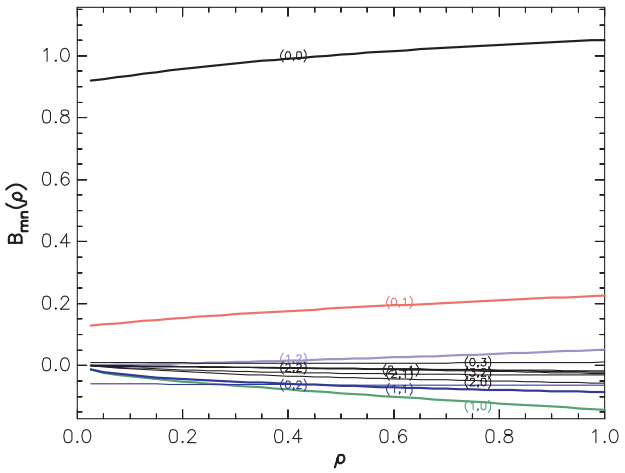

Fig. 4. Dominant components of the QPS magnetic field in field line coordinates.

The degree of quasi-poloidal symmetry decreases on a flux surface from the plasma interior to the edge, as indicated in Fig. 5. Figure 6 shows the ratio of magnetic energy in non-quasi-poloidal modes to that in quasi-poloidal modes vs $(\psi/\psi_{edge})^{1/2} \sim r/a$. However, near the plasma edge these configurations have a more quasi-omnigenous character. Although there has been a large improvement in reducing the non-poloidally symmetric components of the magnetic field since the original two-field-period QPS configuration of September 2000, the newer configurations have about the same degree of poloidal symmetry. Departures from poloidal symmetry can increase neoclassical transport in QPS in much the same way that ripple losses degrade confinement in tokamaks in the low collision frequency regime. Near the edge of QPS, where departures from poloidal symmetry are largest, omnigeneity can reduce the 1/ν transport by producing partial alignment of drift surfaces with magnetic flux surfaces.

Such a departure from exact quasi-poloidal symmetry in QPS is desirable to drive a small, but finite, self-consistent bootstrap current. Typically, the bootstrap current varies from ~30% (at the center) to ~50% (at the edge) of the

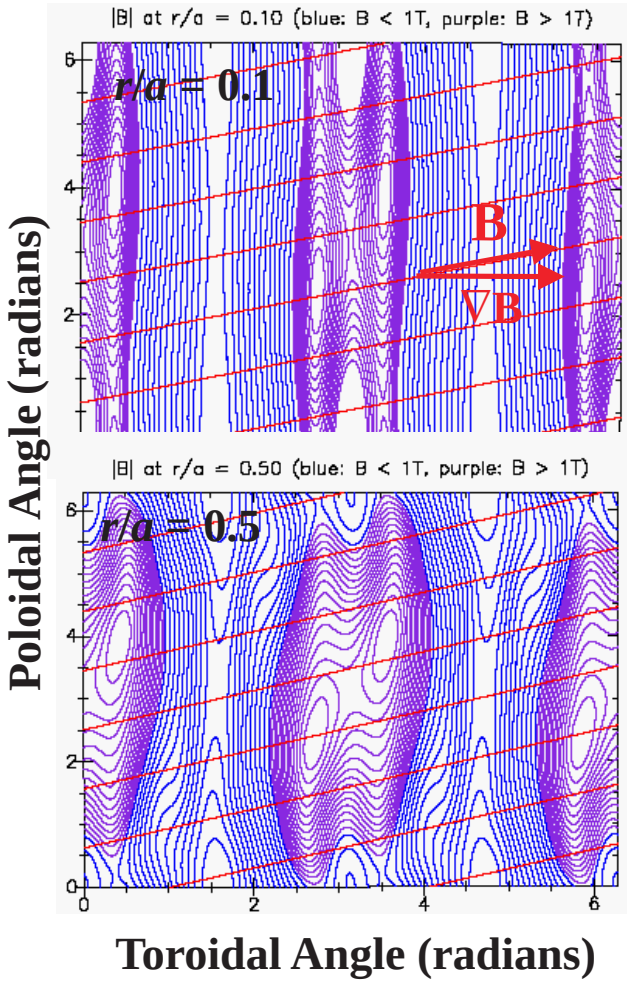

Fig. 5. $|\boldsymbol{B}|$ contours and magnetic field lines on two flux surfaces in QPS.

value that would occur in a tokamak with similar ι profile. The presence of internal bootstrap current at finite β values relieves some of the burden on the coils for producing rotational transform. This reduces the helical excursion of the coils, producing a more compact configuration, and thereby facilitates the engineering of coils at low aspect ratios. In addition, small bootstrap currents can increase ballooning stability limits by reducing unfavorable helical curvature, without introducing vertical or kink modes in the plasma.

The effective ripple ε that should be used in a single-helicity calculation of the low-collisionality 1/ν transport to give the correct neoclassical ripple-induced transport is obtained from the Kernbechler-Nemov NEO code. Figure 7 shows $\varepsilon^{3/2}$ (proportional to the heat diffusivity) for a number of stellarators. As a result of the improvements in the QPS plasma configuration, the low-collisionality neoclassical transport losses have been reduced by a factor of ~15 from the PVR reference configuration; the

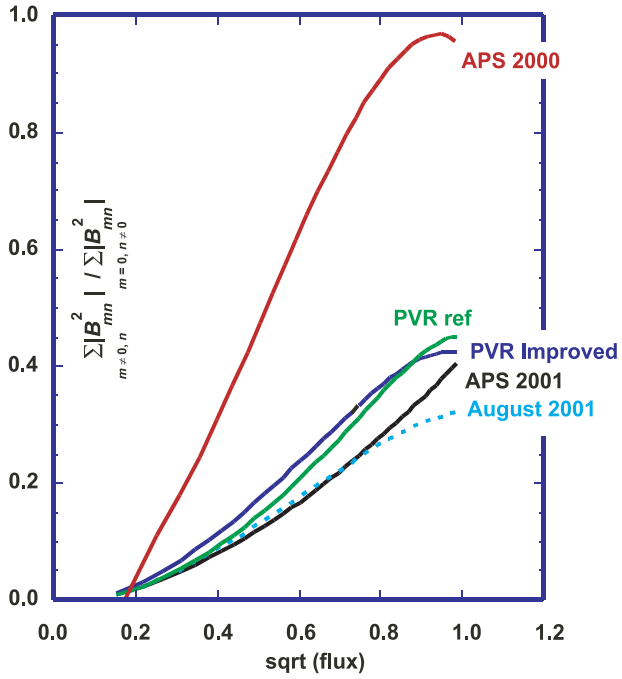

Fig. 6. Energy (B^2) in the non-poloidally symmetric ($m \neq 0$) terms in the $|\boldsymbol{B}|$ Fourier series for different QPS versions.

losses are now at the same level as those in W 7-X, which has an aspect ratio four times that of QPS.

The effect of the improved neoclassical transport on the performance of QPS at low collisionality is illustrated in Fig. 8 for a 1.5-MW ECH plasma at $n_e = 2 \times 10^{19}$ m^{-3}. The 1-D transport calculation includes: (1) anomalous transport corresponding to a factor of 1.5 improvement over the ISS-95 stellarator scaling, and (2) ripple-induced neoclassical transport based on the Shaing-Houlberg model using an equivalent single-helicity QPS ripple corresponding to Fig. 7. The Japanese Large Helical Device and the German Wendelstein 7-AS have obtained up to 2.5 times the ISS-95 confinement. The ripple-induced neoclassical transport component is a perturbation in the power flows at intermediate radii for the QPS configuration whereas it was the dominant component of the power flow for the earlier QPS PVR configuration.

Engineering design improvements

Excellent reconstruction of the optimized LCFS is obtained using the filamentary coils, as shown in Fig. 9. This figure shows cross sections of the LCFS at four toroidal angles for the optimized plasma configuration (dashed curves) and the LCFS obtained from the filamentary coils (solid curves). There is relatively little difference between the optimized and reconstructed LCFS.

The engineering embodiment of the QPS is shown in Fig. 10, which shows a cutaway view of QPS in its bell jar vacuum tank. The modular coil set has two field periods

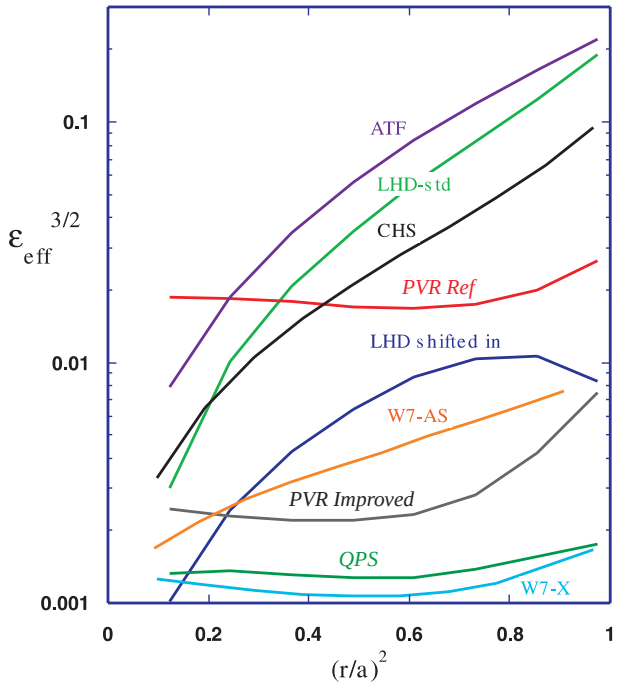

Fig. 7. Relative ripple-induced low-collisionality transport from the NEO code. QPS cases are italicized.

with eight modular coils per period. Because of symmetry, there are only four different coil types. Each of the 16 modular coils has 2 rectangular conductor bundles separated by a stainless steel T. Flexible copper cable conductor would be wound on a form, vacuum impregnated with epoxy, and canned for compatibility with the vacuum. The coil form also allows the coils to be connected into an integral structure. The T is relatively thin for 12 of the coils, but the 2 conductor bundles are more widely separated in the 4 coils in the middle of the long legs of the racetrack configuration, as indicated in Fig. 1. This was done to reduce the errors in reconstructing the optimized field by more than a factor of two. The web between the conductor bundles in these coils can be seen in Fig. 10.

The open space in the central coil bore has been increased to better accommodate the 12 toroidal field (TF) coil legs and the 4 ohmic heating (OH) solenoid windings. The background toroidal field has been increased from ±0.15 T to ±0.2 T, and the Ohmic current capability has been increased from ±50 kA to ±150 kA. The plasma-coil and coil-coil spacings have also been increased. The minimum distance between the LCFS and the modular coil pack is now 9 cm, and the modular coils can now be oriented perpendicular to the coil winding surface for easier fabrication. There is excellent access inside the vacuum vessel for plasma diagnostics and heating. A remaining issue is the need to increase the bend radius of the central modular coils on the inside at the top and bottom. The smaller bend is in the plane of the coils far removed from the plasma, so it should not be difficult to remedy this.

The aluminum spool piece that formed the original cylindrical side of the existing vacuum vessel will be replaced by a stainless steel spool piece. In addition to eliminating eddy currents induced by the poloidal field system, this change (1) allows use of metal seals, instead of differentially pumped Viton seals that can outgas, to yield lower base pressure in the vacuum tank; (2) eliminates the rectangular access door that required differentially pumped viton seals; and (3) allows 12 large (61-cm-diam) ports for diagnostic, heating, and personnel access.

Improved outlook for QPS

The improved QPS configuration is the result of advances in stellarator optimization and coil design codes at ORNL. Incorporation of the Kernbechler-Nemov NEO code into the ORNL stellarator optimization code STELLOPT provided access to QPS designs with improved neoclassical transport. In addition, work on the ORNL drift kinetic equation solver (DKES) transport code has improved its

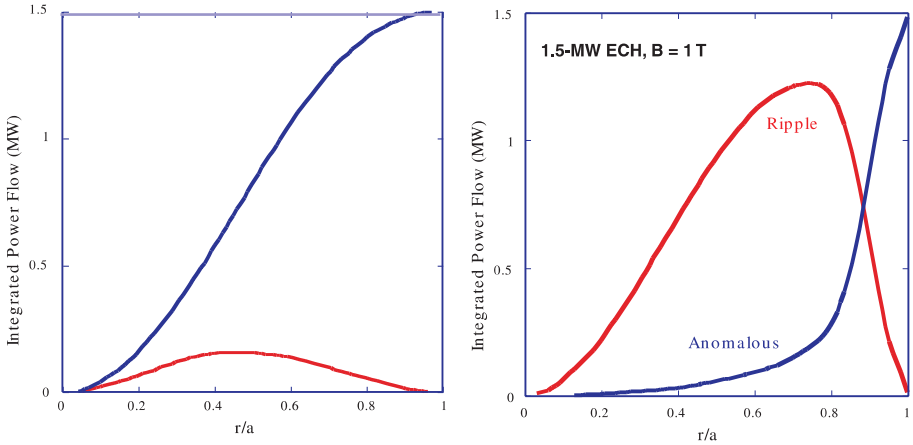

Fig. 8. Integrated power flow through *r/a* for the present QPS configuration (left) and the earlier QPS case (right).

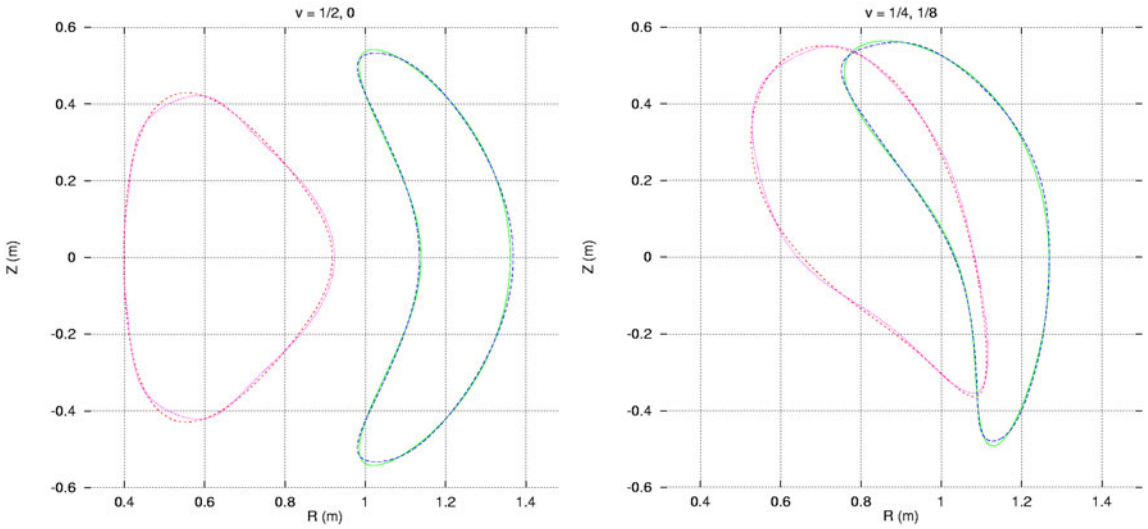

Fig. 9. Reconstruction of the optimized LCFS from the filamentary coils.

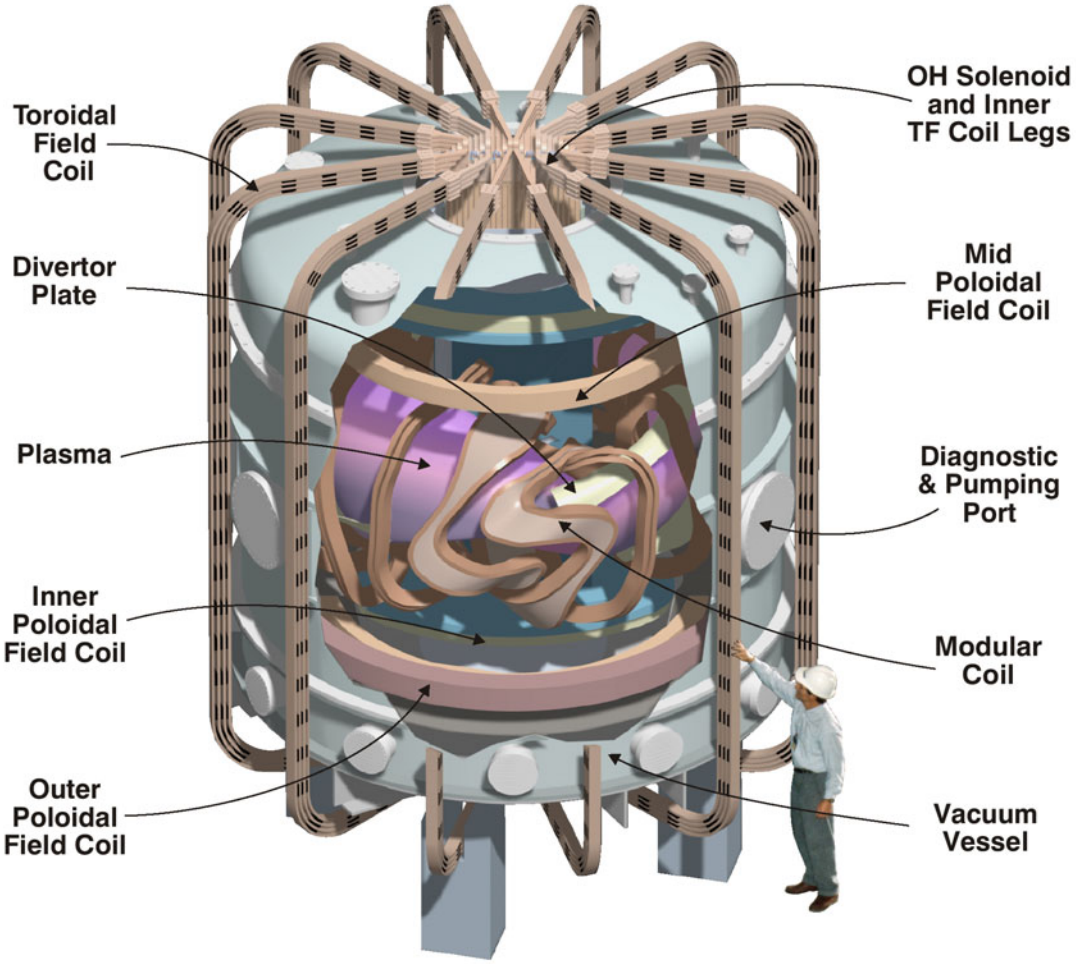

Fig. 10. Cutaway view of QPS in its bell jar vacuum tank

convergence, and therefore its predictive capabilities, in the low-collisionality regime.

Substantial progress has also been made in the development of the ORNL coil design code COILOPT. A major breakthrough in coil development for QPS (and the National Compact Stellarator Experiment, NCSX) has recently been achieved by replacing the global Fourier expansion representation of the modular coils with a local B-spline representation. This allows greater control of local coil bend radii, which is a crucial coil engineering constraint that was previously difficult to control with the Fourier expansion method. For QPS, this spline representation has resulted in much lower magnetic field errors. This allows improved reconstructions of the plasma (from the coils) and preservation of physics properties for the very low R/a QPS configuration. Although further improvements can be expected from using the recently combined STELLOPT and COILOPT codes, which bypasses the intermediate step of finding an optimized LCFS, the present QPS plasma and coil configuration is satisfactory for the more detailed study needed for the May 2002 Conceptual Design Review, the next step in the QPS approval process. The combined STELLOPT/ COILOPT code is now being used to obtain improved coils for NCSX and will be applied to QPS as well.

Work supported by U.S. Dept. of Energy under Contract DE-AC05-00OR22725 with UT-Battelle, LLC.

J. F. Lyon, representing the QPS Team
E-mail: lyonjf@ornl.gov

The QPS Team consists of contributors from
Oak Ridge National Laboratory
University of Texas at Austin
University of Montana
Princeton Plasma Physics Laboratory
Universidad Carlos III de Madrid (Spain)
University of Tennessee at Knoxville